micromachines

MDPI

Article

Numerical Analysis of an Unsteady, Electroviscous, Ternary Hybrid Nanofluid Flow with Chemical Reaction and Activation Energy across Parallel Plates

Muhammad Bilal [1], A. El-Sayed Ahmed [2], Rami Ahmad El-Nabulsi [3,4,5,*], N. Ameer Ahammad [6], Khalid Abdulkhaliq M. Alharbi [7], Mohamed Abdelghany Elkotb [8,9], Waranont Anukool [3,4,5] and Zedan A. S. A. [8,10]

1 Department of Mathematics, City University of Science and Information Technology, Peshawar 25000, KP, Pakistan; bilalchd345@gmail.com
2 Mathematics Department, Faculty of Science, Taif University, P.O. Box 11099, Taif 21944, Saudi Arabia; ahsayed80@hotmail.com
3 Center of Excellence in Quantum Technology, Faculty of Engineering, Chiang Mai University, Chiang Mai 50200, Thailand; waranont.a@cmu.ac.th
4 Research Center for Quantum Technology, Faculty of Science, Chiang Mai University, Chiang Mai 50200, Thailand
5 Department of Physics and Materials Science, Faculty of Science, Chiang Mai University, Chiang Mai 50200, Thailand
6 Department of Mathematics, Faculty of Science, University of Tabuk, P.O. Box 741, Tabuk 71491, Saudi Arabia; anaudalur@ut.edu.sa
7 Mechanical Engineering Department, College of Engineering, Umm Al-Qura University, Makkah 21955, Saudi Arabia; kamharbi@uqu.edu.sa
8 Mechanical Engineering Department, College of Engineering, King Khalid University, Abha 61421, Saudi Arabia; melkotb@kku.edu.sa (M.A.E.); ahafedh@kku.edu.sa (Z.A.S.A.)
9 Mechanical Engineering Department, College of Engineering, Kafrelsheikh University, Kafrelsheikh 33516, Egypt
10 Mechanical Engineering Department, Collage of Engineering at Shoubra, Benha University, Cairo 11629, Egypt
* Correspondence: el-nabulsi@atiner.gr or nabulsiahmadrami@yahoo.fr

check for updates

Citation: Bilal, M.; Ahmed, A.E.-S.; El-Nabulsi, R.A.; Ahammad, N.A.; Alharbi, K.A.M.; Elkotb, M.A.; Anukool, W.; S. A., Z.A. Numerical Analysis of an Unsteady, Electroviscous, Ternary Hybrid Nanofluid Flow with Chemical Reaction and Activation Energy across Parallel Plates. *Micromachines* **2022**, *13*, 874. https://doi.org/10.3390/mi13060874

Academic Editors: Zebing Mao, Jin Xie and Hong Ding

Received: 11 May 2022
Accepted: 28 May 2022
Published: 31 May 2022

Publisher's Note: MDPI stays neutral with regard to jurisdictional claims in published maps and institutional affiliations.

Abstract: Despite the recycling challenges in ionic fluids, they have a significant advantage over traditional solvents. Ionic liquids make it easier to separate the end product and recycle old catalysts, particularly when the reaction media is a two-phase system. In the current analysis, the properties of transient, electroviscous, ternary hybrid nanofluid flow through squeezing parallel infinite plates is reported. The ternary hybrid nanofluid is synthesized by dissolving the titanium dioxide (TiO_2), aluminum oxide (Al_2O_3), and silicon dioxide (SiO_2) nanoparticles in the carrier fluid glycol/water. The purpose of the current study is to maximize the energy and mass transfer rate for industrial and engineering applications. The phenomena of fluid flow is studied, with the additional effects of the magnetic field, heat absorption/generation, chemical reaction, and activation energy. The ternary hybrid nanofluid flow is modeled in the form of a system of partial differential equations, which are subsequently simplified to a set of ordinary differential equations through resemblance substitution. The obtained nonlinear set of dimensionless ordinary differential equations is further solved, via the parametric continuation method. For validity purposes, the outcomes are statistically compared to an existing study. The results are physically illustrated through figures and tables. It is noticed that the mass transfer rate accelerates with the rising values of Lewis number, activation energy, and chemical reaction. The velocity and energy transfer rate boost the addition of ternary NPs to the base fluid.

Keywords: ternary hybrid nanofluids; activation energy; Darcy–Forchheimer flow; electroviscous effect; electric potential; parametric continuation method

1. Introduction

The squeezing flow is important in lubrication equipment, polymer processing, molding compaction, and injection, all of which use hydrodynamical technologies generated from moving surfaces. Jackson [1] highlights the connection between loaded bearings and compressing flow operation in engines, which includes the occurrence of adhesion. Muhammad et al. [2] describe the unsteady squeezed flow of a hybrid nanofluid (HNF), made up of CNTs and CuO, using a numerical technique. The fluid velocity improves as the squeezing intensity and volume fraction of nanomaterials increases. Ramesh et al. [3] explore the unsteady squeezing flow of hydromagnetic and Casson NFs using enclosed parallel disks. Selimefendigil et al. [4] conduct a numerical analysis of nanofluid forced circulation inside a branching channel, under the effect of a constant magnetic flux. Xu et al. [5] study stable power law NF flow, including gyrotactic microorganisms that transmit energy between two parallel plates. Shuaib et al. [6] use 3D flow characteristics to display a 3D NF flow across two contemporaneous circular plates. Their purpose is to see how magnetic induction affects NF flow with heat transmission qualities in the long run. To examine the MHD NF flow through extendable spinning discs, Ahmadian et al. [7] employ the numerical approach bvp4c. The disc stretching process, according to the findings, opposes the flow tendency. Bilal et al. [8] consider the effects of MHD and EHD parameters on the flow of water-based hybrid NFs across two circular plates. With the growing Reynolds number, magnetic, and electric effects, heat transmission is estimated to rise [9,10]. Khan et al. [11] use Fourier's and Fick's laws to explore the channel flow of a second-grade viscoelastic fluid between two plates, formed by a vibrating wall with mass and energy transport characteristics. Alsallami et al. [12] develop an Maxwell nanofluid flow with arrhenius activation energy over a rotating disk. Dawar et al. [13] deploy freshwater as a conventional fluid across two surfaces in order to study copper oxide and copper nanoparticles. The results demonstrate that the particulate concentration factor has a dual influence on velocity distribution. Some recent studies are found in [14–17].

A hybrid nanofluid is a new type of fluid that outperforms when compared to regular fluids, such as ethyl alcohol, water, nanofluids, and ethylene, during energy transitions. HNFs have a huge spectrum of thermal properties, including the ability to freeze at high temperatures [18–20]. Hybrid NFs are used in energy generation, heat transfers, heat pumps, air conditioners, the automotive industry, electrical appliances, turbines, nuclear reactors, broadcasting, spacecraft, and biotechnology [21]. Coolant and freezing solutions containing ethylene glycol and water provide significant advantages, such as reducing corrosion and acid deterioration, as well as suppressing the growth of most bacteria and fungi. In the industry, ethylene glycol and water mixes are referred to as glycol concentrates, mixtures, solutions, and compounds. We employed the TiO_2, SiO_2, and Al_2O_3 NPs in the working fluid in this study. TiO_2 is a white inorganic material that has been used for over a century in a variety of foodstuffs [22]. It is the brightest and whitest pigment known, with reflective qualities, and the ability to absorb and scatter UV radiation [23,24]. Silica is one of the most abundant class of compounds, and because of its inexpensive cost of manufacture, high surface area, and wettability, it has the potential to be an outstanding choice for commercial usage [25,26]. Zhang et al. [27] inspect the entropy maximization in a hydromagnetic HNF flow of SiO2 and (MoS2 (molybdenum disulfide) NPs flowing toward a stretchy surface. Ahmed et al. [28] inspect the Ag–MgO HNF flow with heat propagation generated by a curved spinning disc that rotates in three dimensions, both vertically and horizontally. Chu et al. [29] evaluate flow kinematics and heat transfer from the perspective of TiO_2 and Al_2O_3 NPs used to rise the thermal characteristics of the base fluid. The efficiency of an HNF containing TiO_2 and MWCNTs is analyzed by Chu et al. [30]. Long et al. [31] assess the covalent bonding reactivity of a hybrid ferrofluid flow containing Fe_3O_4 and $CoFe_2O_4$ NPs, in both crosswise and streamwise positions. They made $CoFe_2O_4$ NPs with a well-defined mesoporous dominant structure using hybrid CoFeHCF (hexacyanoferrate) NPs as a substrate. Their research shows a new way to make $CoFe_2O_4$ nano catalysts for pollutant degradation and promotes the usage of CoFeHCF in the ecosystem. Ullah et al. [32] develop

a theoretical formulation for a nonlinear magnetic TiO_2 NF flow through an expanding cylinder Darcy-permeable medium. Shah et al. [33] provide a concise overview of most of $TiO_{2'}$s notable properties, as well as a summary of innovative thermal applications, including its high refractive index, overwhelmingly high boiling and melting points, high stiffness and hardness, ability to absorb or reflect ultraviolet radiation, and photocatalytic nature. Recently, many researchers reported significant contributions to ternary hybrid nanofluid flow [34–37].

Magnetism is one of the key significant features of engineering and drug distribution due to its wide range of applications; heat exchangers, clutches, and compressors, to name a few major commodities, are all modified by the combination of flowing fluid under a magnetic field [38–40]. Magnetic fields have the potential to regulate and make the working temperature of a number of industrial devices more convenient. Magnetic fields are used in interplanetary and extremely high magneto applications, as well as in aerodynamics and chemical chemistry. The strength and scattering of the applied magnetics have an impact on the flow behavior. To describe the flow properties under the upshot of magnetic flux, many researchers committed to fluid mechanics. Hayat et al. [41] look at how specific heat and a produced magnetosphere affected the sinusoidal flow of an HNF flow, via a lateral tube. Raza et al. [42] examine the effect of a molybdenum disulfide nanofluid exchanger and MHD on free convective flow through a channel. Dezfulizadeh et al. [43] explore the performance of MHD ternary HNF flow in a thermal exchanger, using a unique compound-perverted turbulator and spiral rotors. Per the PEC indices, the twisted spinning bar with ellipsoidal surface obstacles has the maximum exergy effectiveness, increasing by 7% in Re, to 12,000. References [44–46] contains some recent literature on MHD HNF.

The present study aimed to numerically examine the cumulative influence of the electromagnetic force, chemical reaction, suction/injection, inertia force, activation energy, ionized fluid, and magnetic field on the squeezing flow of ternary hybrid nanofluids across parallel plates. We supposed that the lower plate is permeable and stretching with a uniform velocity. For this purpose, the phenomena were modeled and formulated in the form of a system of PDEs, which are solved through the parametric continuation method. The results are shown through figures and tables. In the above-described, ionized, ternary nanofluid model, the effects of activation energy, heat source, and chemical reactions in the uses of ternary hybrid nanofluid are the main novelty of the proposed model. Furthermore, in the next section, the problem was articulated, resolved, and discoursed.

2. Governing Equations

The ternary hybrid nanofluid flow across two parallel infinite plates, consisting of titanium dioxide, silicon dioxide, and aluminum oxide is reported. The flow mechanism is graphically depicted in Figure 1. The upper plate is located at $y = h(t) = \sqrt{\frac{(1-\alpha t)\nu_{bf}}{b}}$, which fluctuates downwards with the velocity $\frac{dh}{dt} = \frac{-\alpha}{2}\sqrt{\frac{\nu_{bf}}{b(1-\alpha t)}}$. The lower plate is permeable, which allows suction/injection effect, signified as $V_w = \frac{-V_0}{(1-\alpha t)}$. Both plates are assumed at constant temperatures T_1 and T_2. The lower plate is expanding with the linear velocity $u_w = \frac{-bx}{(1-\alpha t)}$. Furthermore, the time-dependent magnetic field is characterized as $H = \frac{B_0}{(1-\alpha t)}$. The basic flow equations are communicated as [47–49]:

$$\frac{\partial u}{\partial x} + \frac{\partial v}{\partial y} = 0, \tag{1}$$

$$\frac{\partial U}{\partial t} + u\frac{\partial U}{\partial x} + v\frac{\partial U}{\partial y} = \frac{\mu_{hnf}}{\rho_{hnf}}\frac{\partial^2 U}{\partial y^2} - \frac{\sigma_{hnf}}{\rho_{hnf}}H^2 U - \frac{\mu_{hnf}}{\rho_{hnf}}\frac{U}{K^*} - FrU^2 - \left(n^+ - n^-\right)\frac{BK^2\mu_{hnf}}{\rho_{hnf}}\frac{\partial W}{\partial x}, \tag{2}$$

$$\frac{\partial^2 W}{\partial x^2} + \frac{\partial^2 W}{\partial y^2} = \frac{K}{2}\left(n^+ - n^-\right), \tag{3}$$

$$\frac{\partial n^+}{\partial t} + u\frac{\partial n^+}{\partial x} + v\frac{\partial n^+}{\partial y} = \frac{\mu_{hnf}}{\rho_{hnf} Sc}\left(\frac{\partial^2 n^+}{\partial y^2} + \frac{\partial W}{\partial x}\frac{\partial n^+}{\partial x} + \frac{\partial W}{\partial y}\frac{\partial n^+}{\partial y} + n^+\frac{\partial^2 W}{\partial y^2}\right), \quad (4)$$

$$\frac{\partial n^-}{\partial t} + u\frac{\partial n^-}{\partial x} + v\frac{\partial n^-}{\partial y} = \frac{\mu_{hnf}}{\rho_{hnf} Sc}\left(\frac{\partial^2 n^-}{\partial y^2} + \frac{\partial W}{\partial x}\frac{\partial n^-}{\partial x} + \frac{\partial W}{\partial y}\frac{\partial n^-}{\partial y} + n^-\frac{\partial^2 W}{\partial y^2}\right), \quad (5)$$

$$\frac{\partial T}{\partial t} + u\frac{\partial T}{\partial x} + v\frac{\partial T}{\partial y} = \frac{K_{hnf}}{(\rho C_p)_{hnf}}\frac{\partial^2 T}{\partial y^2} + \frac{Q_0}{(\rho C_p)_{hnf}}(T - T_0), \quad (6)$$

$$\frac{\partial C}{\partial t} + u\frac{\partial C}{\partial x} + v\frac{\partial C}{\partial y} = D_B\frac{\partial^2 C}{\partial y^2} + \frac{D_T}{T_1}\frac{\partial^2 T}{\partial y^2} - k_r^2(C - C_0)\left(\frac{T}{T_\infty}\right)^n \exp\left(-\frac{E_a}{\kappa T}\right). \quad (7)$$

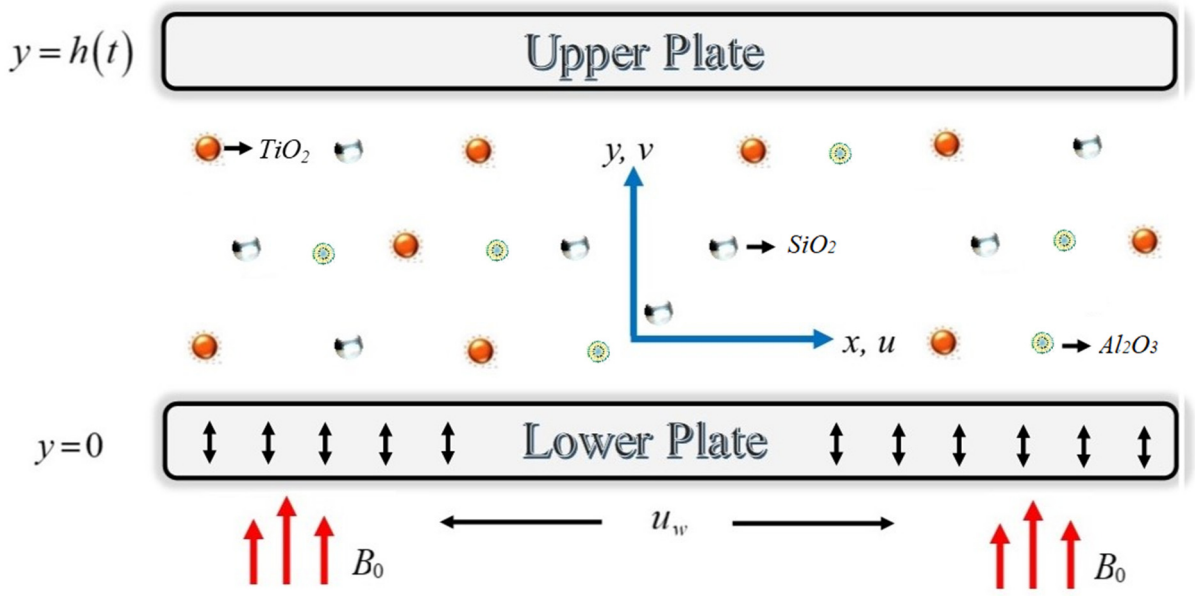

Figure 1. Electroviscous fluid flow across two parallel plates.

Equation (1) is the continuity equation, Equation (2) is the momentum equation with electroviscous and uniform magnetic effect, Equation (3) is the Poisson equation, Equations (4) and (5) are Nernst–Planck equations, while Equations (6) and (7) are the energy and mass distribution equations, respectively.

In Equations (1)–(7), n^- and n^+ are the negative and positive charged ions; $U = \frac{\partial v}{\partial x} - \frac{\partial u}{\partial y}$ are the associate's condition for the upper and lower plate; T and C are the temperature and the concentration, respectively; $Fr = \frac{C_b^*}{\sqrt{K^*}}$ is the porous media non-inertial coefficient, where K^* and C_b^* are the permeability factor and drag force constant, respectively; Q_0 is the heat generation term; $K^2 = \frac{2z^2e^2n_0}{\varepsilon_0 \varepsilon k_b T}$ is the inverse Debye factor; W is the electric potential of ions; and $B = \frac{\rho k^2 T^2 \varepsilon_0 \varepsilon}{2z^2e^2\mu^2}$ is fixed at a constant temperature. E_a is the activation energy, and k_T is the chemical reaction rate. Furthermore, $(\rho C_p)_{Thnf}$, μ_{Thnf}, σ_{Thnf}, κ_{Thnf} and ρ_{Thnf} are the heat capacity, dynamic viscosity, electrical conductivity, thermal conductivity, and density of ternary HNF, respectively.

The boundary conditions are:

$$\begin{aligned} &u = \lambda_1\frac{bx}{(1-\alpha t)}, \quad v = -\frac{V_0}{(1-\alpha t)}, \quad T = T_1, \quad C = C_1, \quad W = 0, \quad n^- = n^+ = 0 \quad \text{at} \quad y = 0 \\ &u = 0, \quad v = -\frac{dh(t)}{dt}, \quad T = T_2, \quad C = C_2, \quad W = \frac{x}{l^2(1-\alpha t)}, \quad n^- = n^+ = \frac{\alpha}{\nu_{b_f}(1-\alpha t)} \quad \text{at} \quad y = h(t). \end{aligned} \quad (8)$$

The similarity variables are:

$$\begin{array}{l}\Psi=\sqrt{\frac{bv_{bf}}{(1-\alpha t)}}x\,f(\eta),\ \ u=\frac{bx}{(1-\alpha t)}f'(\eta),\ \ v\ =-\sqrt{\frac{bv_{bf}}{(1-\alpha t)}}f(\eta),\ \ \theta(\eta)=\frac{T-T_1}{T_2-T_1},\ \ \phi(\eta)=\frac{C-C_1}{C_2-C_1},\\ W=\frac{x}{l^2(1-\alpha t)}P(\eta),\quad n^-=\frac{\alpha}{v_{bf}(1-\alpha t)}H(\eta),\quad n^+=\frac{\alpha}{v_{bf}(1-\alpha t)}G(\eta),\quad \eta=y\sqrt{\frac{b}{v_{bf}(1-\alpha t)}}.\end{array} \tag{9}$$

Therefore, the transformed set of ODEs is:

$$f^{iv}=\frac{\vartheta_1}{\vartheta_2}\left(\frac{Sq}{2}\left(\eta f'''+3f'\right)-ff'''+f'f''-Frf''^2\right)-\frac{\vartheta_3}{\vartheta_2}Mf''+K_1^*f''+BK^2RH(G-H), \tag{10}$$

$$p''=-\frac{1}{2}K^2\delta_1(G-H), \tag{11}$$

$$g''=\frac{\vartheta_1}{\vartheta_2}\left(\frac{Sq}{2}\left(\eta g'+2g\right)-fg'\right)Sc-\frac{1}{\delta_1}\left(g'p'-\frac{K^2\delta_1}{2}\left(g^2-gh\right)\right), \tag{12}$$

$$h''=\frac{\vartheta_1}{\vartheta_2}\left(\frac{Sq}{2}\left(\eta h'+2h\right)-fh'\right)Sc-\frac{1}{\delta_1}\left(h'p'-\frac{K^2\delta_1}{2}\left(gh-h^2\right)\right), \tag{13}$$

$$\theta''=\frac{\vartheta_4}{\vartheta_{35}}\left(\frac{Sq\ Pr}{2}\eta\theta'-Prf\theta'-\frac{Pr}{\vartheta_4}Q\theta\right), \tag{14}$$

$$\phi''=\frac{Sq\ Le}{2}\eta\phi'-Lef\phi'-\frac{Nt}{Nb}\frac{\vartheta_4}{\vartheta_5}\left(\frac{Sq\ Pr}{2}\eta\theta'-Prf\theta'-\frac{Pr}{\vartheta_4}Q\theta\right)-Sc\sigma(1+\delta\theta)^n\phi\ \ \exp\left(-\frac{E}{1+\delta\theta}\right). \tag{15}$$

Here, $\vartheta_1=\frac{\rho_{Thnf}}{\rho_{bf}}$, $\vartheta_2=\frac{\mu_{Thnf}}{\mu_{bf}}$, $\vartheta_3=\frac{\sigma_{Thnf}}{\sigma_{bf}}$, $\vartheta_4=\frac{(\rho Cp)_{Thnf}}{(\rho Cp)_{bf}}$, $\vartheta_5=\frac{\kappa_{Thnf}}{\kappa_{bf}}$. M is the magnetic term, Pr is the Prandtl number, Sq is the squeezing constraint, K_1^* is the local porosity term, λ > 0 is the stretching parameter for the lower plate (λ = 0) for the fixed plate), Fr is the Forchheimer number, Sc is the Schmidt number, Nt is the thermophoresis constant, S is the suction/injection term, Le is the Lewis number, Q is the heat source/sink term, Nb is the Brownian motion constant, E is the Arrhenius activation energy coefficient, and σ is the chemical reaction term, defined as:

$$\begin{array}{l}M=\frac{\sigma_{bf}B_0^2}{b\rho_{bf}},\ \ Pr=\frac{\mu_{bf}Cp_{bf}}{\kappa_{bf}},\ \ Sq=\frac{\alpha}{b},\ \ K_1^*=\frac{v_{bf}(1-\alpha t)}{K^*b},\ \ Sc=\frac{\mu_{bf}}{\rho_{bf}D},\ \ Nt=\frac{D_T(T_2-T_1)}{T_1v_{bf}},\\ S=\frac{V_0}{lb},\ \ Le=\frac{v_{bf}}{D_B},\ \ \delta_1=\frac{\alpha^2}{l^2},\ \ Q=\frac{Q_0}{b\left(\rho C_p\right)_{bf}},\ \ Nb=\frac{D_B(C_2-C_1)}{v_{bf}},\ \ E=\frac{E_a}{\kappa T_\infty},\ \ \sigma=\frac{k_T^2}{c}.\end{array} \tag{16}$$

The transform boundary conditions are:

$$\left.\begin{array}{l}f'(0)=\lambda,\ \ f(0)=S,\ \ \theta(0)=\delta,\ \ \phi(0)=\omega,\ \ p(0)=0,\ \ g(0)=0,\ \ h(0)=0\quad at\quad y=0\\ f'(1)=0,\ \ f(1)=\frac{Sq}{2},\ \ \theta(1)=1,\ \ \phi(1)=1,\ \ p(1)=1,\ \ h(1)=1,\ \ g(1)=1\quad at\quad y=1.\end{array}\right\} \tag{17}$$

The Nusselt number and the skin friction are characterized as:

$$\left.\begin{array}{ll}Re_x^{1/2}C_{f_u}=\frac{\mu_{Thnf}}{\mu_{bf}}f''(1), & Re_x^{1/2}C_{f_l}=\frac{\mu_{Thnf}}{\mu_{bf}}f''(0),\\ Re_x^{-1/2}N_{u_u}=-\frac{\kappa_{Thnf}}{\kappa_{bf}}\theta'(1), & Re_x^{-1/2}N_{u_l}=-\frac{\kappa_{Thnf}}{\kappa_{bf}}\theta'(0).\end{array}\right\} \tag{18}$$

where $Re_x=\frac{xU_w}{v_{bf}}$.

3. Numerical Solution

This section shows how to use the algorithm of the numerical scheme to solve the numerical solutions of the suggested mathematical model. The main steps for dealing with the parametric continuation method scheme and future direction are as follows [50–57]:

Step 1: Simplifying the modeled equations to 1st order:

$$\left.\begin{array}{l} \hbar_1 = f, \quad \hbar_2 = f', \quad \hbar_3 = f'', \quad \hbar_4 = f''', \quad \hbar_5 = p, \quad \hbar_6 = p', \quad \hbar_7 = g, \\ \hbar_8 = g', \quad \hbar_9 = h, \quad \hbar_{10} = h', \quad \hbar_{11} = \theta, \quad \hbar_{12} = \theta', \quad \hbar_{13} = \phi, \quad \hbar_{14} = \phi'. \end{array}\right\} \tag{19}$$

By putting Equation (19) in Equations (10)–(15) and (17), we achieve:

$$\hbar'_4 = \frac{\vartheta_1}{\vartheta_2}\left(\frac{Sq}{2}(\eta\hbar_4 + 3\hbar_2) - \hbar_1\hbar_4 + \hbar_2\hbar_3 - Fr\hbar_3^2\right) - \frac{\vartheta_3}{\vartheta_2}Mf'' + K_1^*\hbar_3 + BK^2R\hbar_9(\hbar_7 - \hbar_9), \tag{20}$$

$$\hbar'_6 = -\frac{1}{2}K^2\delta_1(\hbar_7 - \hbar_9), \tag{21}$$

$$\hbar'_8 = \frac{\vartheta_1}{\vartheta_2}\left(\frac{Sq}{2}(\eta\hbar_8 + 2\hbar_7) - \hbar_1\hbar_8\right)Sc - \frac{1}{\delta_1}\left(\hbar_8\hbar_6 - \frac{K^2\delta_1}{2}\left({\hbar_7}^2 - \hbar_7\hbar_9\right)\right), \tag{22}$$

$$\hbar'_{10} = \frac{\vartheta_1}{\vartheta_2}\left(\frac{Sq}{2}(\eta\hbar_{10} + 2\hbar_9) - \hbar_1\hbar_{10}\right)Sc - \frac{1}{\delta_1}\left(\hbar_{10}\hbar_6 - \frac{K^2\delta_1}{2}\left(\hbar_7\hbar_9 - {\hbar_9}^2\right)\right), \tag{23}$$

$$\hbar'_{12} = \frac{\vartheta_4}{\vartheta_{35}}\left(\frac{Sq\ Pr}{2}\eta\hbar_{12} - Pr\hbar_1\hbar_{12} - \frac{Pr}{\vartheta_4}Q\hbar_{11}\right), \tag{24}$$

$$\hbar'_{14} = \frac{Sq\ Le}{2}\eta\hbar_{14} - Le\hbar_1\hbar_{14} - \frac{Nt}{Nb}\frac{\vartheta_4}{\vartheta_5}\begin{pmatrix} \frac{Sq\ Pr}{2}\eta\hbar_{12} - Pr \\ \hbar_1\hbar_{12} - \frac{Pr}{\vartheta_4}Q\hbar_{11} \end{pmatrix} - Sc\sigma(1+\delta\theta)^n\hbar_{13}\ \exp\left(-\frac{E}{1+\delta\hbar_{11}}\right). \tag{25}$$

with the corresponding boundary conditions:

$$\left.\begin{array}{l} \hbar_2(0) = \lambda, \ \hbar_1(0) = S, \ \hbar_{11}(0) = \delta, \ \hbar_{13}(0) = \omega, \ \hbar_5(0) = 0, \ \hbar_7(0) = 0, \ \hbar_9(0) = 0 \quad at \quad y = 0 \\ \hbar_2(1) = 0, \ \hbar_1(1) = \frac{Sq}{2}, \ \hbar_{11}(1) = 1, \ \hbar_{13}(1) = 1, \ \hbar_5(1) = 1, \ \hbar_7(1) = 1, \ \hbar_9(1) = 1 \quad at \quad y = 1. \end{array}\right\} \tag{26}$$

Step 2: Introducing the embedding parameter p:

$$\hbar'_4 = \frac{\vartheta_1}{\vartheta_2}\left(\frac{Sq}{2}(\eta\hbar_4 + 3\hbar_2) - \hbar_1(\hbar_4 - 1)p + \hbar_2\hbar_3 - Fr\hbar_3^2\right) - \frac{\vartheta_3}{\vartheta_2}Mf'' + K_1^*\hbar_3 + BK^2R\hbar_9(\hbar_7 - \hbar_9), \tag{27}$$

$$\hbar'_6 = -\frac{1}{2}K^2\delta_1(\hbar_7 - \hbar_9), \tag{28}$$

$$\hbar'_8 = \frac{\vartheta_1}{\vartheta_2}\left(\frac{Sq}{2}(\eta\hbar_8 + 2\hbar_7) - \hbar_1(\hbar_8 - 1)p\right)Sc - \frac{1}{\delta_1}\left(\hbar_8\hbar_6 - \frac{K^2\delta_1}{2}\left({\hbar_7}^2 - \hbar_7\hbar_9\right)\right), \tag{29}$$

$$\hbar'_{10} = \frac{\vartheta_1}{\vartheta_2}\left(\frac{Sq}{2}(\eta\hbar_{10} + 2\hbar_9) - \hbar_1(\hbar_{10} - 1)p\right)Sc - \frac{1}{\delta_1}\left(\hbar_{10}\hbar_6 - \frac{K^2\delta_1}{2}\left(\hbar_7\hbar_9 - {\hbar_9}^2\right)\right), \tag{30}$$

$$\hbar'_{12} = \frac{\vartheta_4}{\vartheta_{35}}\left(\frac{Sq\ Pr}{2}\eta\hbar_{12} - Pr\hbar_1(\hbar_{12} - 1)p - \frac{Pr}{\vartheta_4}Q\hbar_{11}\right), \tag{31}$$

$$\hbar'_{14} = \frac{Sq\ Le}{2}\eta(\hbar_{14} - 1)p - Le\hbar_1\hbar_{14} - \frac{Nt}{Nb}\frac{\vartheta_4}{\vartheta_5}\begin{pmatrix} \frac{Sq\ Pr}{2}\eta\hbar_{12} - Pr \\ \hbar_1\hbar_{12} - \frac{Pr}{\vartheta_4}Q\hbar_{11} \end{pmatrix} - Sc\sigma(1+\delta\theta)^n\hbar_{13}\ \exp\left(-\frac{E}{1+\delta\hbar_{11}}\right). \tag{32}$$

Step 3: Differentiating by parameter 'p':

$$V' = \mathbb{A}V + R, \tag{33}$$

where $\mathbb{A}$ is the coefficient matrix.

$$V = \frac{d\hbar_i}{d\tau} \tag{34}$$

where i = 1, 2, . . . , 11.

Step 4: Apply the Cauchy principal:

$$V = aU + W, \tag{35}$$

where W and U are the indefinite vector functions.

$$U' = aU, \tag{36}$$

$$W' = \mathbb{A}W + R, \tag{37}$$

By putting the approximate solution Equation (26) into the original Equation (24), we obtain:

$$(aU + W)' = \mathbb{A}(aU + W) + R, \tag{38}$$

Step 5: Solving the Cauchy problems:

$$\frac{U^{i+1} - U^i}{\Delta\eta} = \mathbb{A}U^{i+1}, \quad \frac{W^{i+1} - W^i}{\Delta\eta} = \mathbb{A}W^{i+1}. \tag{39}$$

Finally, we obtain:

$$U^{i+1} = (I - \Delta\mathbb{A}\eta)^{-1}U^i, \qquad W^{i+1} = (I - \Delta\mathbb{A}\eta)^{-1}(W^i + \Delta\eta R). \tag{40}$$

4. Results and Discussion

This section reveals the physical description of the obtained results in form of figures and tables for velocity, energy, and mass transfer profiles versus several physical constraints. The default parametric values used for the simulation of modeled equations are: $\phi_1 = \phi_2 = \phi_3 = 0.01$, $S = 1.0$, $Fr = 0.5$, $S = 1.0$ & -1.0, $Sc = 0.1$, $Le = 0.4$, $Sq = 0.5$, $E = 1.0$, $M = 0.3$, $Nt = Nb = 0.1$, $\sigma = 0.5$, and $Q = 0.2$. The following observations are noticed.

Velocity Profile ($f'(\eta)$):

Figure 2a–e displays the tendency of velocity profile($f'(\eta)$) versus suction parameter $S > 0$, Darcy–Forchheimer Fr, magnetic field M, injection $S < 0$, and volume friction of ternary nanoparticles $\Psi = (\phi_1 = \phi_2 = \phi_3)$, respectively. Figure 2a–c shows that the velocity field is lessened with the upshot of suction parameter, Darcy–Forchheimer, and magnetic field. Physically, the rising effect of the suction factor diminishes the motion of fluid particles, which causes a reduction in the velocity profile, as shown in Figure 2a. The permeability of the plate surface enhances with the variation of the Darcy effect, which also encourages more suction from the plate surface and, as a result, fluid velocity ($f'(\eta)$) declines, as depicted in Figure 2b. The resistive force, which is created due to the magnetic effect M, opposes the fluid motion, similarly also deducing the velocity boundary layer, as shown in Figure 2c.

Figure 2d,e illustrate that the velocity distribution accelerates with the flourishing values of injection and volume friction of ternary nanoparticles. Physically, due to the injection effect of fluid particles, the fluid moves fast; as a consequence, the velocity of fluid flow elevates, as elaborated in Figure 2d. The addition of ternary nanoparticles (TiO_2, SiO_2, Al_2O_3) to the base fluid magnifies its thermal conduction, which also causes the inclination in the velocity field, as revealed in Figure 2e.

Electric Field ($g(\eta)$, $h(\eta)$):

Figure 3a–d report the presentation of the electric field ($g(\eta)$, $h(\eta)$) profile versus the Schmidt number Sc, and squeezing term Sq, respectively. The kinetic viscosity of fluid enhances with the effect of the Schmidt number, which diminishes the molecular dissemination, and causes the lessening of the electric field ($g(\eta)$, $h(\eta)$), as shown in Figure 3a,b. The influence of the squeezing variable fluctuates the fluid particles, which enhances its velocity, and as a result, the electric profile is also boosted, as elaborated in Figure 3c,d.

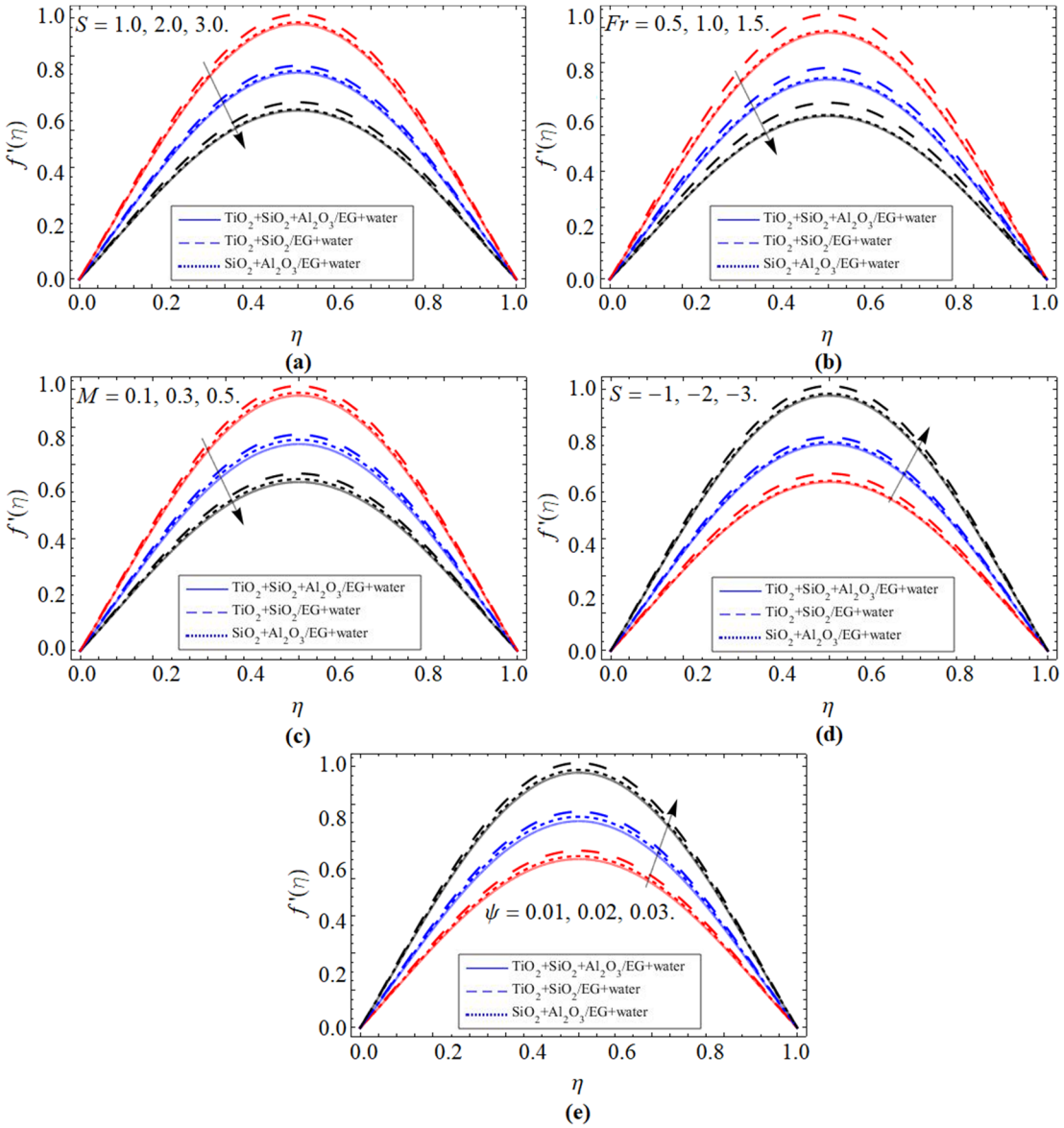

Figure 2. The tendency of velocity profile ($f'(\eta)$) versus (**a**) suction term $S > 0$, (**b**) Darcy–Forchheimer Fr, (**c**) magnetic field M, (**d**) injection $S < 0$, and (**e**) volume friction of ternary nanoparticles $\Psi = (\phi_1 = \phi_2 = \phi_3)$.

Energy Profile $\theta(\eta)$:

Figure 4a–c represents the tendency of energy profile $\theta(\eta)$ versus the heat source Q, volume friction of ternary nanoparticles Ψ, and injection $S < 0$ constraints, respectively. As a consequence of the heat generation term, thermal energy is generated inside the fluid flow, which causes the elevation of the energy profile $\theta(\eta)$, as seen in Figure 4a. Figure 4b illustrates that the inclusion of nanomaterials (TiO_2, SiO_2, Al_2O_3) in the base fluid augments the thermal conduction of the base fluid, as well as reduces the average heat capacity, because the specific heat capacity of ethylene glycol/water is much higher than ternary nanoparticles. This is why the energy propagation rate of ternary nanofluid magnifies with the rising quantity in the concentration of nanoparticles Ψ. The energy transfer rate of ternary NFs declines with the upshot of the injection term, as shown in Figure 4c.

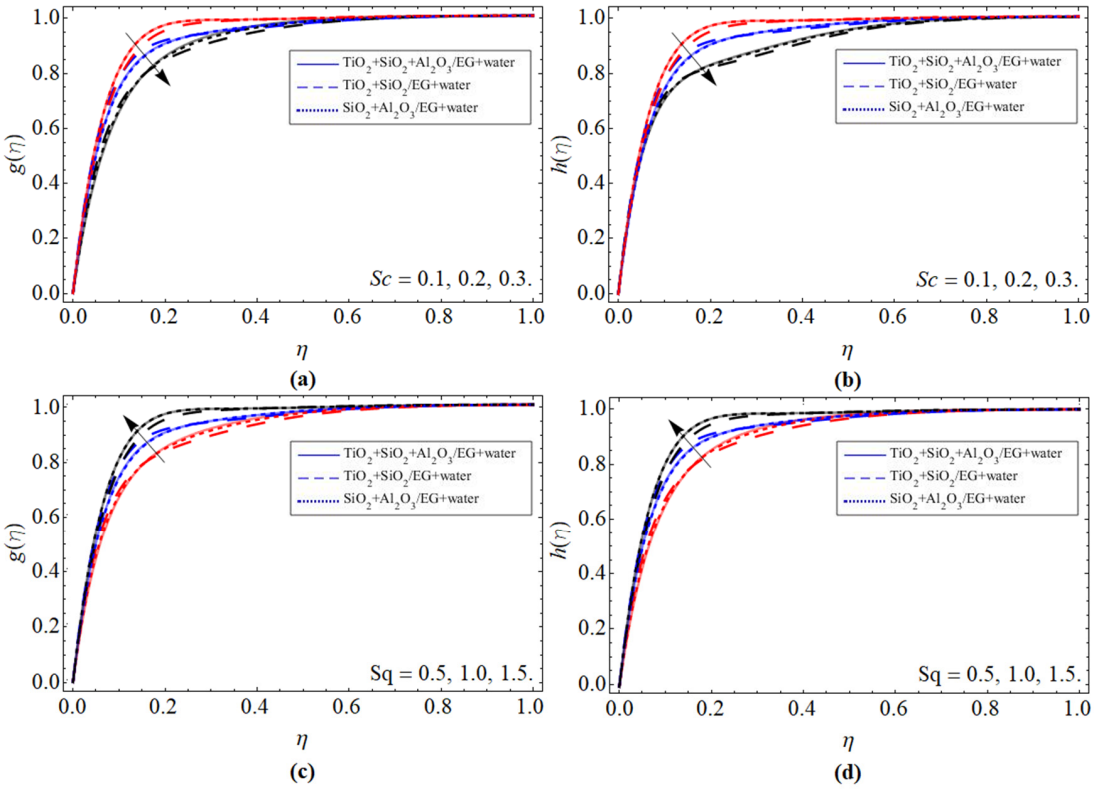

Figure 3. The tendency of electric field ($g(\eta)$, $h(\eta)$) versus (**a**,**b**) Schmidt number Sc, (**c**,**d**) squeezing term Sq.

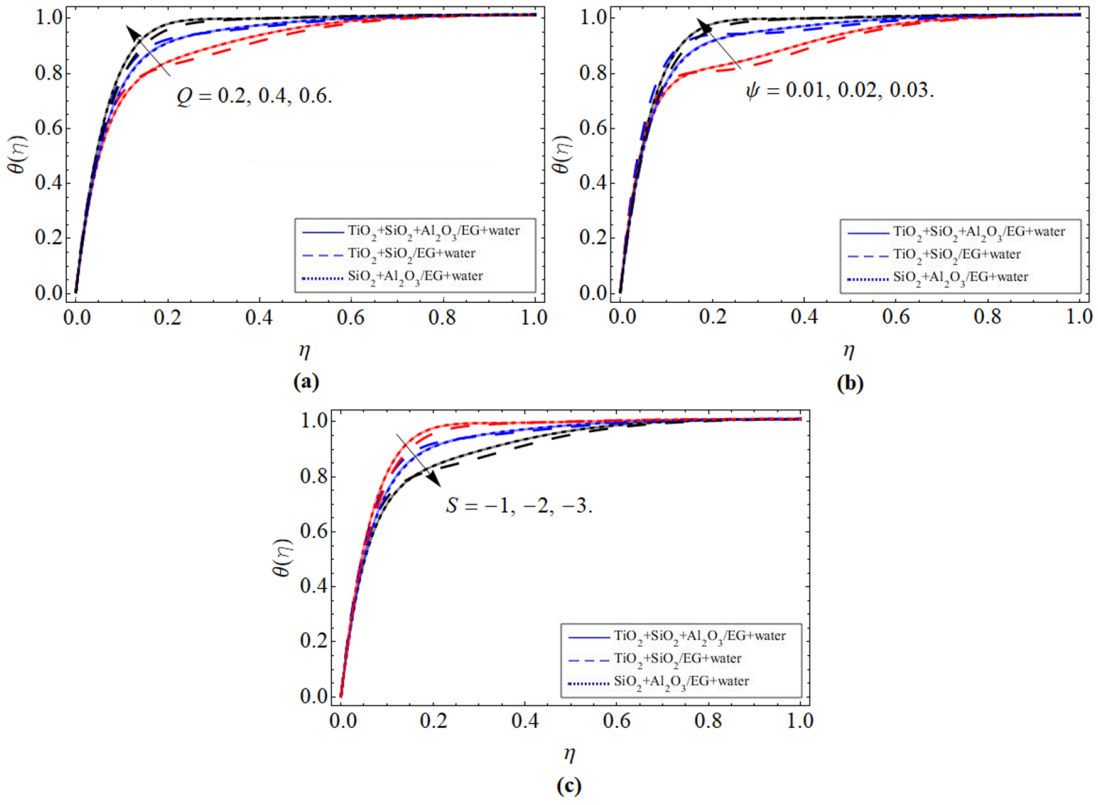

Figure 4. The tendency of energy profile $\theta(\eta)$ versus (**a**) heat source Q, (**b**) volume friction of ternary nanoparticles Ψ, and (**c**) injection $S < 0$.

Mass Profile $\phi(\eta)$:

Figure 5a–e displays the trend of mass profile $\phi(\eta)$ versus *Le*, *Nt*, *Nb*, activation energy *E*, and chemical reaction rate σ, respectively. Figure 5a–c elaborates that the transfer rate boosts with the rising values of Lewis number, which remarkably declines with the upshot of *Nt* and *Nb*. Physically, the molecular diffusion rate reduces with the variation of *Le*, which results in the reduction in the concentration boundary layer, as seen in Figure 5a. Furthermore, we are interested in investigating the influence of *Nb* and *Nt* on the flow mechanism, as these are two important factors that govern nanofluid movement. Brownian motion is a haphazard motion occurring as a result of nanomaterials in a fluid flow. Brownian motion is more powerful in fluids with low viscosity and elevated heat, as well as in fluids with tiny particles. However, their effect reduces the mass proportion ratio, as manifested in Figure 5b,c. The increment in activation energy constraint *E* and chemical reaction term dramatically elevate the mass transmission ratio, as publicized in Figure 5d,e. The effect of both factors accelerates the kinetic energy inside the fluid, which encourages fluid particles to move fast; as a result, the concentration profile of ternary nanofluid enhances.

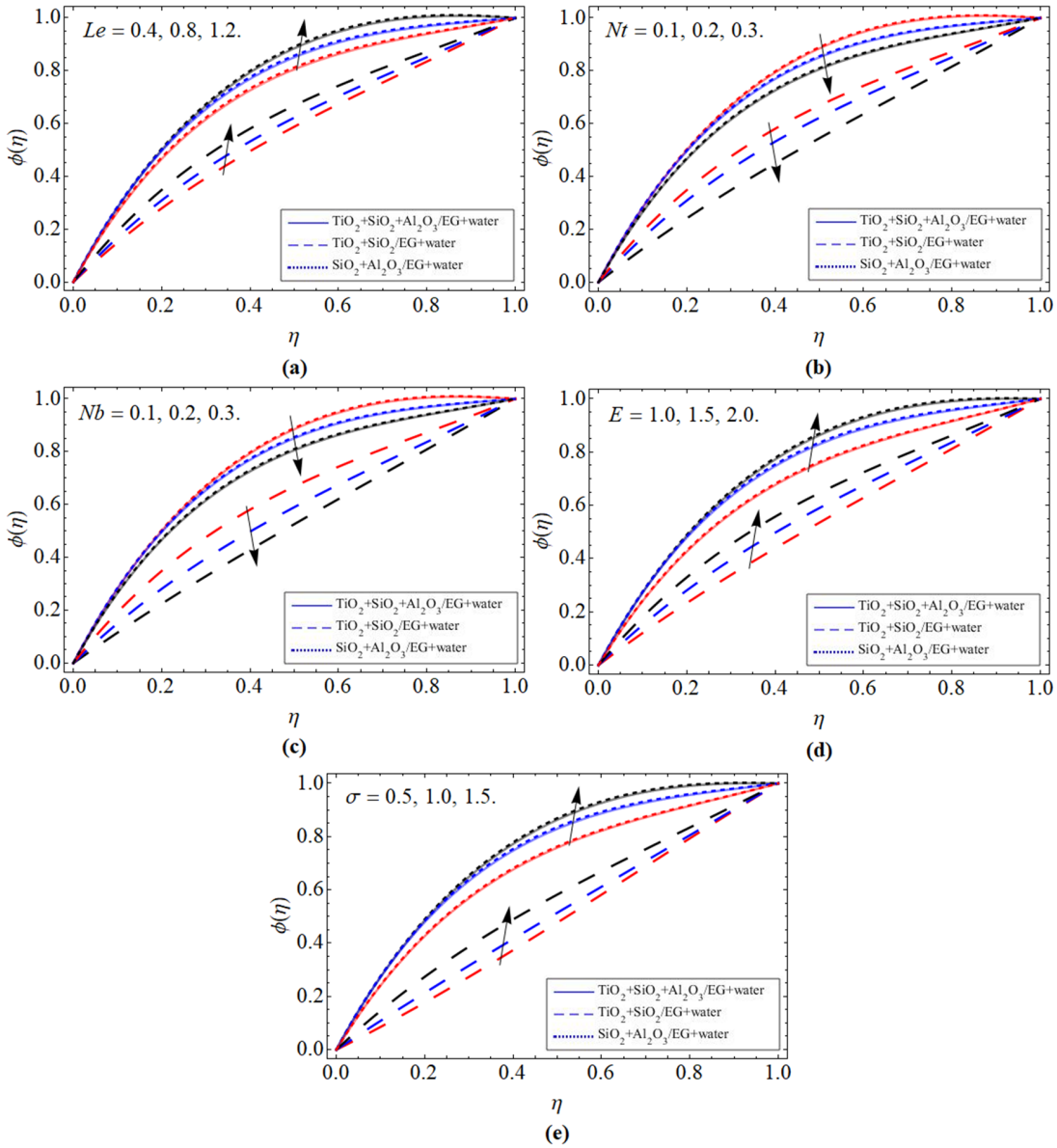

Figure 5. The tendency of mass profile $\phi(\eta)$ versus (**a**) Lewis number *Le*, (**b**) thermophoresis term *Nt*, (**c**) Brownian motion *Nb*, (**d**) activation energy *E*, and (**e**) chemical reaction rate σ.

Tables 1 and 2 expose the experimental values of the base fluid (ethylene glycol/water) and ternary nanoparticles (TiO_2, SiO_2, Al_2O_3), and the physical model of ternary hybrid nanofluid, respectively. Table 3 reveals the statistical assessment of current results with the available work for validity purposes. It is perceived that both results show the best settlement. Furthermore, the influence of magnetic term and suction constraints enhances the skin friction of both the upper and lower plate. Table 4 exhibits the comparative valuation of present outcomes with the published literature for the Nusselt number $-(\theta'(1))$.

Table 1. The experimental values of silicon dioxide $(\phi_1 = \phi_{SiO_2})$, titanium dioxide $(\phi_2 = \phi_{TiO_2})$ and aluminum oxide $(\phi_3 = \phi_{Al_2O_3})$ [58].

Base Fluid & Nanoparticles	ρ (kg/m^3)	k (W/mK))	Cp (j/kg K)	σ (S/m)
$C_2H_6O_2$-H_20	1063.8	0.387	3630	0.00509
TiO_2	4250	8.953	686.2	2.38×10^6
SiO_2	2270	1.4013	3630	3.5×10^6
Al_2O_3	6310	32.9	773	5.96×10^7

Table 2. The physical model for ternary hybrid nanofluid [23].

Viscosity	$\frac{\mu_{Thnf}}{\mu_f} = \frac{1}{(1-\phi_{SiO_2})^{2.5}(1-\phi_{TiO_2})^{2.5}(1-\phi_{Al_2O_3})^{2.5}}$,
Density	$\frac{\rho_{Thnf}}{\rho_f} = (1-\phi_{TiO_2})\left[(1-\phi_{TiO_2})\left\{(1-\phi_{Al_2O_3}) + \phi_{Al_2O_3}\frac{\rho_{Al_2O_3}}{\rho_f}\right\} + \phi_{TiO_2}\frac{\rho_{TiO_2}}{\rho_f}\right] + \phi_{SiO_2}\frac{\rho_{SiO_2}}{\rho_f}$,
Specific heat	$\frac{(\rho cp)_{Thnf}}{(\rho cp)_f} = \phi_{SiO_2}\frac{(\rho cp)_{SiO_2}}{(\rho cp)_f} + (1-\phi_{SiO_2})\left[\begin{array}{l}(1-\phi_{TiO_2})\left\{(1-\phi_{Al_2O_3}) + \phi_{Al_2O_3}\frac{(\rho cp)_{Al_2O_3}}{(\rho cp)_f}\right\} \\ +\phi_{TiO_2}\frac{(\rho cp)_{TiO_2}}{(\rho cp)_f}\end{array}\right]\Bigg\}$
Thermal conduction	$\left.\begin{array}{l}\frac{k_{Thnf}}{k_{hnf}} = \left(\frac{k_{Al_2O_3}+2k_{hnf}-2\phi_{Al_2O_3}(k_{hnf}-k_{Al_2O_3})}{k_{Al_2O_3}+2k_{hnf}+\phi_{Al_2O_3}(k_{hnf}-k_{Al_2O_3})}\right), \frac{k_{hnf}}{k_{nf}} = \left(\frac{k_{TiO_2}+2k_{nf}-2\phi_{TiO_2}(k_{nf}-k_{TiO_2})}{k_{TiO_2}+2k_{nf}+\phi_{TiO_2}(k_{nf}-k_{TiO_2})}\right), \\ \frac{k_{nf}}{k_f} = \left(\frac{k_{SiO_2}+2k_f-2\phi_{SiO_2}(k_f-k_{SiO_2})}{k_{SiO_2}+2k_f+\phi_{SiO_2}(k_f-k_{SiO_2})}\right),\end{array}\right\}$
Electrical conductivity	$\left.\begin{array}{l}\frac{\sigma_{Thnf}}{\sigma_{hnf}} = \left[1+\frac{3\left(\frac{\sigma_{Al_2O_3}}{\sigma_{hnf}}-1\right)\phi_{Al_2O_3}}{\left(\frac{\sigma_{Al_2O_3}}{\sigma_{hnf}}+2\right)-\left(\frac{\sigma_{Al_2O_3}}{\sigma_{hnf}}-1\right)\phi_{Al_2O_3}}\right], \frac{\sigma_{hnf}}{\sigma_{nf}} = \left[1+\frac{3\left(\frac{\sigma_{TiO_2}}{\sigma_{nf}}-1\right)\phi_{TiO_2}}{\left(\frac{\sigma_{TiO_2}}{\sigma_{nf}}+2\right)-\left(\frac{\sigma_{TiO_2}}{\sigma_{nf}}-1\right)\phi_{TiO_2}}\right], \\ \frac{\sigma_{nf}}{\sigma_f} = \left[1+\frac{3\left(\frac{\sigma_{SiO_2}}{\sigma_f}-1\right)\phi_{SiO_2}}{\left(\frac{\sigma_{SiO_2}}{\sigma_f}+2\right)-\left(\frac{\sigma_{SiO_2}}{\sigma_f}-1\right)\phi_{SiO_2}}\right]\end{array}\right\}$

Table 3. The comparative assessment of present outcomes with the published literature for upper and lower plate skin friction $(f''(1), f''(0))$.

Parameters		$f''(1)$		$f''(0)$	
M	S	Khashi'ie et al. [47]	Present Work	Khashi'ie et al. [47]	Present Work
0.0	0.5	4.7132028	4.7132043	−7.4101525	−7.4101542
1.0		4.7391165	4.7391176	−7.5906177	−7.5906188
4.0		4.8201511	4.8201533	−8.1113342	−8.1113363
9.0		4.9647698	4.9647787	−8.9110956	−8.9110978
	0.0	1.8423469	1.8423476	−4.5868911	−4.5868933
	0.3	3.6535948	3.6535969	−6.6646620	−6.6646632
	0.6	5.3911475	5.3911494	−8.8524442	−8.8524453
	1.0	7.5933262	7.5933283	−11.9475843	−11.9475941

Table 4. The comparative assessment of present outcomes with the published literature for Nusselt number $-(\theta'(1))$.

Parameter	Khan et al. [59] (Numerical)	Present Work	Khan et al. [59] (Analytic)	Present Work
Sq	$-(\theta'(1))$	$-(\theta'(1))$	$-(\theta'(1))$	$-(\theta'(1))$
0.0	−0.8443	−0.8452	−0.8438	−0.8445
0.2	−0.8791	−0.8880	−0.8783	−0.8794
0.4	−0.9151	−0.9162	−0.9140	−0.9153
0.6	−0.9523	−0.9542	−0.9511	−0.9532
0.8	−0.9908	−0.9916	−0.9914	−0.9935
1.0	−1.0306	−1.0317	−1.0310	−1.0332

5. Conclusions

We studied the properties of transient, electroviscous, ternary hybrid nanofluid flow through squeezing parallel infinite plates. The ternary HNF was manufactured by adding the TiO_2, SiO_2, and Al_2O_3 to the conventional fluid glycol/water. The ternary hybrid nanofluid flow was modeled in the form of the system of partial differential equations, which were subsequently simplified to a set of ODEs through resemblance substitution. The obtained nonlinear set of dimensionless ODEs is further solved via the parametric continuation method. The key findings are:

- The velocity field $f'(\eta)$ is reduced with the effect of the suction parameter, Darcy–Forchheimer, and magnetic field.
- The flourishing values of injection and volume friction of ternary nanoparticles (TiO_2, SiO_2, Al_2O_3) accelerate the velocity distribution.
- The electric field ($g(\eta)$, $h(\eta)$) declines with the upshot of Schmidt number Sc, while enhancing with the increment of squeezing term Sq.
- The thermal energy field $\theta(\eta)$ is elevated versus the variation of heat source and the inclusion of nanomaterials to the base fluid, while reducing with injection effect.
- The mass allocation rate boosts with the rising values of Lewis number, activation energy constraint E, and chemical reaction, while declines with the upshot of thermophoresis and Brownian motion.

Author Contributions: Conceptualization, M.B. and R.A.E.-N.; data curation, A.E.-S.A., K.A.M.A. and M.A.E.; formal analysis, M.B., N.A.A., K.A.M.A. and M.A.E.; formal analysis, R.A.E.-N.; investigation, M.B., A.E.-S.A., K.A.M.A. and W.A.; methodology, M.B., N.A.A., M.A.E., W.A. and Z.A.S.A.; resources, Z.A.S.A.; software, A.E.-S.A., N.A.A. and Z.A.S.A.; supervision, R.A.E.-N. and W.A.; validation, R.A.E.-N. All authors have read and agreed to the published version of the manuscript.

Funding: This research received no external funding.

Data Availability Statement: The data that supports the findings of this study are available within the article.

Acknowledgments: The authors extend their appreciation to the Deanship of Scientific Research at King Khalid University, Abha, Saudi Arabia, for funding this work through the Research Group Program under grant no. RGP. 2/19/43. The El-Sayed Ahmed would like to thank Taif University Researchers supporting Project number (TURSP-2020/159), Taif University, Saudi Arabia. The authors would like to thank the Deanship of Scientific Research at Umm Al-Qura University for supporting this work by Grant Code: (22UQU4310392DSR10). Rami Ahmad El-Nabulsi would like to thank sincerely Annette Li, assistant editor of Micromachines, for her support and her free discount for the present work. We thank the anonymous reviewers for their careful reading of our manuscript and their many insightful comments and suggestions.

Conflicts of Interest: The authors declare no conflict of interest.

References

1. Jackson, J. A Study of Squeezing Flow. *Appl. Sci. Res. Sec. A* **1963**, *11*, 148–152. [CrossRef]
2. Muhammad, K.; Hayat, T.; Alsaedi, A.; Ahmad, B. Melting Heat Transfer in Squeezing Flow of Basefluid (Water), Nanofluid (CNTs+ Water) and Hybrid Nanofluid (CNTs+ CuO+ Water). *J. Therm. Anal. Calorim.* **2021**, *143*, 1157–1174. [CrossRef]
3. Eiamsa-Ard, S.; Wongcharee, K.; Sripattanapipat, S. 3-D Numerical Simulation of Swirling Flow and Convective Heat Transfer in a Circular Tube Induced by Means of Loose-Fit Twisted Tapes. *Int. Commun. Heat Mass Transf.* **2009**, *36*, 947–955. [CrossRef]
4. Selimefendigil, F.; Öztop, H.F.; Chamkha, A.J. Role of Magnetic Field on Forced Convection of Nanofluid in a Branching Channel. *Int. J. Numer. Methods Heat Fluid Flow* **2019**, *30*, 1755–1772. [CrossRef]
5. Xu, Y.-J.; Bilal, M.; Al-Mdallal, Q.; Khan, M.A.; Muhammad, T. Gyrotactic Micro-Organism Flow of Maxwell Nanofluid between Two Parallel Plates. *Sci. Rep.* **2021**, *11*, 15142. [CrossRef]
6. Shuaib, M.; Bilal, M.; Qaisar, S. Numerical Study of Hydrodynamic Molecular Nanoliquid Flow with Heat and Mass Transmission between Two Spinning Parallel Plates. *Phys. Scr.* **2020**, *96*, 025201. [CrossRef]
7. Ahmadian, A.; Bilal, M.; Khan, M.A.; Asjad, M.I. The non-Newtonian Maxwell Nanofluid Flow between Two Parallel Rotating Disks under the Effects of Magnetic Field. *Sci. Rep.* **2020**, *10*, 17088. [CrossRef]
8. Bilal, M.; Gul, T.; Alsubie, A.; Ali, I. Axisymmetric Hybrid Nanofluid Flow with Heat and Mass Transfer amongst the Two Gyrating Plates. *ZAMM–J. Appl. Math. Mech./Z. Angew. Math. Mech.* **2021**, *101*, e202000146. [CrossRef]
9. Chu, Y.-M.; Shankaralingappa, B.; Gireesha, B.; Alzahrani, F.; Khan, M.I.; Khan, S.U. Combined Impact of Cattaneo-Christov Double Diffusion and Radiative Heat Flux on Bio-Convective Flow of Maxwell Liquid Configured by a Stretched Nano-Material Surface. *Appl. Math. Comput.* **2022**, *419*, 126883. [CrossRef]
10. Zhao, T.H.; Khan, M.I.; Chu, Y.M. Artificial Neural Networking (ANN) Analysis for Heat and Entropy Generation in Flow of Non-Newtonian Fluid between Two Rotating Disks. *Math. Methods Appl. Sci.* **2021**. [CrossRef]
11. Khan, Z.; Ali, F.; Andualem, M. Free Convection Flow of Second Grade Dusty Fluid between Two Parallel Plates using Fick's and Fourier's Laws: A Fractional Model. *Sci. Rep.* **2022**, *12*, 3448. [CrossRef] [PubMed]
12. Alsallami, S.A.; Zahir, H.; Muhammad, T.; Hayat, A.U.; Khan, M.R.; Ali, A. Numerical Simulation of Marangoni Maxwell Nanofluid Flow with Arrhenius Activation Energy and Entropy Anatomization over a Rotating Disk. *Waves Random Complex Media* **2022**, 1–19. [CrossRef]
13. Dawar, A.; Saeed, A.; Kumam, P. Magneto-Hydrothermal Analysis of Copper and Copper Oxide Nanoparticles between Two Parallel Plates with Brownian Motion and Thermophoresis Effects. *Int. Commun. Heat Mass Transf.* **2022**, *133*, 105982. [CrossRef]
14. Chamkha, A.J. On Laminar Hydromagnetic Mixed Convection Flow in a Vertical Channel with Symmetric and Asymmetric wall Heating Conditions. *Int. J. Heat Mass Transf.* **2002**, *45*, 2509–2525. [CrossRef]
15. Singh, R.; Bishnoi, J.; Tyagi, V.K. Triple Diffusive Convection with Soret–Dufour Effects in a Maxwell Nanofluid Saturated in a Darcy Porous Medium. *SN Appl. Sci.* **2020**, *2*, 704. [CrossRef]
16. Darbari, A.M.; Alavi, M.A.; Saleh, S.R.; Nejati, V. Sensitivity Analysis of Nanofluid Flow over Different Flat Tubes Confined between two Parallel Plates using Taguchi Method and Statistical Analysis of Variance. *Int. J. Therm. Sci.* **2022**, *173*, 107428. [CrossRef]
17. Vickers, N.J. Animal Communication: When i'm calling you, will you answer too? *Curr. Biol.* **2017**, *27*, R713–R715. [CrossRef]
18. Zhou, S.-S.; Bilal, M.; Khan, M.A.; Muhammad, T. Numerical Analysis of Thermal Radiative Maxwell Nanofluid Flow over-stretching Porous Rotating Disk. *Micromachines* **2021**, *12*, 540. [CrossRef]
19. Alhowaity, A.; Hamam, H.; Bilal, M.; Ali, A. Numerical Study of Williamson Hybrid Nanofluid Flow with Thermal Characteristics past over an Extending Surface. *Heat Transf.* **2022**, 1–15. [CrossRef]
20. Al-Mubaddel, F.S.; Allehiany, F.M.; Nofal, T.A.; Alam, M.M.; Ali, A.; Asamoah, J.K.K. Rheological Model for Generalized Energy and Mass Transfer through Hybrid Nanofluid Flow Comprised of Magnetized Cobalt Ferrite Nanoparticles. *J. Nanomater.* **2022**. [CrossRef]
21. Ullah, I.; Hayat, T.; Alsaedi, A. Optimization of Entropy Production in Flow of Hybrid Nanomaterials through Darcy–Forchheimer Porous Space. *J. Therm. Anal. Calorim.* **2021**, *147*, 5855–5864. [CrossRef]
22. Elattar, S.; Helmi, M.M.; Elkotb, M.A.; El-Shorbagy, M.; Abdelrahman, A.; Bilal, M.; Ali, A. Computational Assessment of Hybrid Nanofluid Flow with the Influence of Hall Current and Chemical Reaction over a Slender Stretching Surface. *Alex. Eng. J.* **2022**, *61*, 10319–10331. [CrossRef]
23. Alharbi, K.A.M.; Ahmed, A.E.-S.; Ould Sidi, M.; Ahammad, N.A.; Mohamed, A.; El-Shorbagy, M.A.; Bilal, M.; Marzouki, R. Computational Valuation of Darcy Ternary-Hybrid Nanofluid Flow across an Extending Cylinder With Induction Effects. *Micromachines* **2022**, *13*, 588. [CrossRef] [PubMed]
24. Ullah, Z.; Ullah, I.; Zaman, G.; Sun, T.C. A Numerical Approach to Interpret Melting and Activation Energy Phenomenon on the Magnetized Transient Flow of Prandtl–Eyring Fluid with the Application of Cattaneo–Christov Theory. *Waves Random Complex Media* **2022**, 1–21. [CrossRef]
25. Nguyen, Q.; Rizvandi, R.; Karimipour, A.; Malekahmadi, O.; Bach, Q.-V. A Novel Correlation to Calculate Thermal Conductivity of Aqueous Hybrid Graphene Oxide/Silicon Dioxide Nanofluid: Synthesis, Characterizations, Preparation, and Artificial Neural Network Modeling. *Arab. J. Sci. Eng.* **2020**, *45*, 9747–9758. [CrossRef]

26. Khan, M.I.; Khan, S.A.; Hayat, T.; Waqas, M.; Alsaedi, A. Modeling and Numerical Simulation for Flow of Hybrid Nanofluid ($SiO_2/C_3H_8O_2$) and ($MoS_2/C_3H_8O_2$) with Entropy Optimization and Variable Viscosity. *Int. J. Numer. Methods Heat Fluid Flow* **2019**, *22*, 3939–3955. [CrossRef]
27. Zhang, X.-H.; Algehyne, E.A.; Alshehri, M.G.; Bilal, M.; Khan, M.A.; Muhammad, T. The Parametric Study of Hybrid Nanofluid Flow with Heat Transition Characteristics over a Fluctuating Spinning Disk. *PLoS ONE* **2021**, *16*, e0254457. [CrossRef]
28. Ahmed, J.; Shahzad, A.; Farooq, A.; Kamran, M.; Ud-Din Khan, S.; Ud-Din Khan, S. Thermal Analysis in Swirling Flow of Titanium Dioxide–Aluminum Oxide Water Hybrid Nanofluid over a Rotating Cylinder. *J. Therm. Anal. Calorim.* **2021**, *144*, 2175–2185. [CrossRef]
29. Chu, Y.M.; Bashir, S.; Ramzan, M.; Malik, M.Y. Model-Based Comparative Study of Magnetohydrodynamics Unsteady Hybrid Nanofluid Flow between Two Infinite Parallel Plates with Particle Shape Effects. *Math. Methods Appl. Sci.* **2022**. [CrossRef]
30. Chu, Y.-M.; Nazir, U.; Sohail, M.; Selim, M.M.; Lee, J.-R. Enhancement in Thermal Energy and Solute Particles using Hybrid Nanoparticles by Engaging Activation Energy and Chemical Reaction over a Parabolic Surface via Finite Element Approach. *Fract. Fract.* **2021**, *5*, 119. [CrossRef]
31. Long, X.; Yang, S.; Qiu, X.; Ding, D.; Feng, C.; Chen, R.; Wang, X.; Chen, N.; Lei, Q. Heterogeneous Activation of Peroxymonosulfate for Bisphenol A Degradation using $CoFe_2O_4$ Derived by Hybrid Cobalt-Ion Hexacyanoferrate Nanoparticles. *Chem. Eng. J.* **2021**, *404*, 127052. [CrossRef]
32. Ullah, I.; Hayat, T.; Alsaedi, A.; Asghar, S. Dissipative Flow of Hybrid Nanoliquid (H_2O-Aluminum Alloy Nanoparticles) with Thermal Radiation. *Phys. Scr.* **2019**, *94*, 125708. [CrossRef]
33. Shah, T.R.; Zhou, C.; Ali, H.M. Titanium Dioxide: Advancements and Thermal Applications. In *Titanium Dioxide*; Ali, H.M., Ed.; IntechOpen Limited: London, UK, 2022. [CrossRef]
34. Ullah, I.; Hayat, T.; Aziz, A.; Alsaedi, A. Significance of Entropy Generation and the Coriolis Force on the Three-Dimensional Non-Darcy Flow of Ethylene-Glycol Conveying Carbon Nanotubes (SWCNTs and MWCNTs). *J. Non-Equilib. Thermodyn.* **2022**, *47*, 61–75. [CrossRef]
35. Bilal, M.; Saeed, A.; Gul, T.; Ali, I.; Kumam, W.; Kumam, P. Numerical Approximation of Microorganisms Hybrid Nanofluid Flow Induced by a Wavy Fluctuating Spinning Disc. *Coatings* **2021**, *11*, 1032. [CrossRef]
36. Algehyne, E.A.; Alhusayni, Y.Y.; Tassaddiq, A.; Saeed, A.; Bilal, M. The Study of Nanofluid Flow with Motile Microorganism and Thermal Slip Condition across a Vertical Permeable Surface. *Waves Random Complex Media* **2022**, 1–18. [CrossRef]
37. Bilal, M.; Saeed, A.; Gul, T.; Kumam, W.; Mukhtar, S.; Kumam, P. Parametric Simulation of Micropolar Fluid with Thermal Radiation Across a Porous Stretching Surface. *Sci. Rep.* **2022**, *12*, 2542. [CrossRef]
38. Bilal, M.; Ayed, H.; Saeed, A.; Brahmia, A.; Gul, T.; Kumam, P. The Parametric Computation of Nonlinear Convection Magnetohydrodynamic Nanofluid Flow with Internal Heating across a Fixed And Spinning Disk. *Waves Random Complex Media* **2022**, 1–16. [CrossRef]
39. Ullah, I. Activation Energy with Exothermic/Endothermic Reaction and Coriolis Force Effects on Magnetized Nanomaterials Flow through Darcy–Forchheimer Porous Space with Variable Features. *Waves Random Complex Media* **2022**, 1–14. [CrossRef]
40. Gul, T.; Khan, A.; Bilal, M.; Alreshidi, N.A.; Mukhtar, S.; Shah, Z.; Kumam, P. Magnetic Dipole Impact on the Hybrid Nanofluid Flow over an Extending Surface. *Sci. Rep.* **2020**, *10*, 8474. [CrossRef]
41. Hayat, T.; Noreen, S. Peristaltic Transport of Fourth Grade Fluid with Heat Transfer and Induced Magnetic Field. *C. R. Mec.* **2010**, *338*, 518–528. [CrossRef]
42. Raza, J.; Mebarek-Oudina, F.; Chamkha, A. Magnetohydrodynamic flow of molybdenum disulfide nanofluid in a channel with shape effects. *Multidiscip. Modeling Mater. Struct.* **2019**, *15*, 737. [CrossRef]
43. Dezfulizadeh, A.; Aghaei, A.; Hassani Joshaghani, A.; Najafizadeh, M.M. Exergy Efficiency of a Novel Heat Exchanger under MHD Effects Filled with Water-Based Cu–SiO_2-MWCNT Ternary Hybrid Nanofluid based on Empirical Data. *J. Therm. Anal. Calorim.* **2021**, *147*, 4781–4804. [CrossRef]
44. Yuvaraj, T.; Ravi, K. Multi-Objective Simultaneous DG and DSTATCOM Allocation in Radial Distribution Networks using Cuckoo Searching Algorithm. *Alex. Eng. J.* **2018**, *57*, 2729–2742. [CrossRef]
45. Krishna, M.V.; Chamkha, A.J. Hall and Ion Slip Effects on MHD Rotating Flow of Elastico-Viscous Fluid through Porous Medium. *Int. Commun. Heat Mass Transf.* **2020**, *113*, 104494. [CrossRef]
46. Krishna, M.V.; Ahamad, N.A.; Chamkha, A.J. Hall and Ion Slip Impacts on Unsteady MHD Convective Rotating Flow of Heat Generating/Absorbing Second Grade Fluid. *Alex. Eng. J.* **2021**, *60*, 845–858. [CrossRef]
47. Khashi'ie, N.S.; Waini, I.; Arifin, N.M.; Pop, I. Unsteady Squeezing Flow of Cu-Al_2O_3/Water Hybrid Nanofluid in a Horizontal Channel with Magnetic Field. *Sci. Rep.* **2021**, *11*, 14128. [CrossRef]
48. Khan, M.S.; Shah, R.A.; Ali, A.; Khan, A. Parametric Investigation of the Nernst–Planck Model and Maxwell's Equations for a Viscous Fluid between Squeezing Plates. *Bound. Value Probl.* **2019**, *2019*, 107. [CrossRef]
49. Khan, M.S.; Shah, R.A.; Khan, A. Effect of Variable Magnetic Field on the Flow between Two Squeezing Plates. *Eur. Phys. J. Plus* **2019**, *134*, 219. [CrossRef]
50. Nazeer, M.; Hussain, F.; Khan, M.I.; El-Zahar, E.R.; Chu, Y.-M.; Malik, M. Theoretical Study of MHD Electro-Osmotically Flow of Third-Grade Fluid in Micro Channel. *Appl. Math. Comput.* **2022**, *420*, 126868. [CrossRef]

51. Shahi, A.M.; Issac, B.; Modapothala, J.R. Intelligent Corporate Sustainability Report Scoring Solution using Machine Learning Approach to Text Categorization. In Proceedings of the 2012 IEEE Conference on Sustainable Utilization and Development in Engineering and Technology (STUDENT), Kuala Lumpur, Malaysia, 6–9 October 2012; pp. 227–232.
52. Zhao, T.; Wang, M.; Chu, Y. Monotonicity and Convexity Involving Generalized Elliptic Integral of the First Kind. *Revista de la Real Academia de Ciencias Exactas, Físicas y Naturales Serie A Matemáticas* **2021**, *115*, 46. [CrossRef]
53. Shuaib, M.; Shah, R.A.; Bilal, M. Variable Thickness Flow over a Rotating Disk under the Influence of Variable Magnetic Field: An Application to Parametric Continuation Method. *Adv. Mech. Eng.* **2020**, *12*, 1687814020936385. [CrossRef]
54. Zhao, T.-H.; Zhou, B.-C.; Wang, M.-K.; Chu, Y.-M. On Approximating the Quasi-Arithmetic Mean. *J. Inequal. Appl.* **2019**, *2019*, 42. [CrossRef]
55. Zhao, T.-H.; Wang, M.-K.; Zhang, W.; Chu, Y.-M. Quadratic Transformation Inequalities for Gaussian Hypergeometric Function. *J. Inequal. Appl.* **2018**, *2018*, 251. [CrossRef] [PubMed]
56. Rashid, S.; Sultana, S.; Karaca, Y.; Khalid, A.; Chu, Y.-M. Some Further Extensions Considering Discrete Proportional Fractional Operators. *Fractals* **2022**, *30*, 2240026. [CrossRef]
57. Wang, F.; Khan, M.N.; Ahmad, I.; Ahmad, H.; Abu-Zinadah, H.; Chu, Y.-M. Numerical Solution of Traveling Waves in Chemical Kinetics: Time-Fractional Fishers Equations. *Fractals* **2022**, *30*, 2240051. [CrossRef]
58. Manjunatha, S.; Puneeth, V.; Gireesha, B.; Chamkha, A. Theoretical Study of Convective Heat Transfer in Ternary Nanofluid Flowing past a Stretching Sheet. *J. Appl. Comput. Mech.* **2021**. [CrossRef]
59. Khan, M.S.; Mei, S.; Fernandez-Gamiz, U.; Noeiaghdam, S.; Khan, A. Numerical Simulation of a Time-Dependent Electroviscous and Hybrid Nanofluid with Darcy-Forchheimer Effect between Squeezing Plates. *Nanomaterials* **2022**, *12*, 876. [CrossRef]